JPhys Energy

PURPOSE-LED PUBLISHING™

PAPER • OPEN ACCESS

Unravelling composition and mass-loading effects in monolithic non-stoichiometric silicon nitride anodes for lithium-ion batteries

To cite this article: Alestair Wilson *et al* 2026 *J. Phys. Energy* **8** 015028

Journal of Physics: Energy

OPEN ACCESS

RECEIVED
30 November 2025

REVISED
31 January 2026

ACCEPTED FOR PUBLICATION
25 February 2026

PUBLISHED
6 March 2026

PAPER

Unravelling composition and mass-loading effects in monolithic non-stoichiometric silicon nitride anodes for lithium-ion batteries

Alestair Wilson[1,3], **Thomas A McKnelly**[1,3], **Sowmya Ramachandran**[1], **Paula Perez Rodriguez**[1], **Prasad Gonugunta**[2], **Peyman Taheri**[2], **Olindo Isabella**[1], **René van Swaaij**[1,*] **and Moumita Rana**[1,*]

[1] Photovoltaic Materials and Devices group, Delft University of Technology, Mekelweg 4, 2628 CD Delft, The Netherlands
[2] Materials Science and Engineering group, Delft University of Technology, Mekelweg 2, 2628 CD Delft, The Netherlands
[3] These authors contributed equally to this manuscript.
[*] Authors to whom any correspondence should be addressed.

E-mail: r.a.c.m.m.vanswaaij@tudelft.nl and m.rana@tudelft.nl

Keywords: lithium-ion battery, silicon anode, monolithic electrodes, anode failure mechanism, anode optimization, thin-film anodes

Supplementary material for this article is available online

Abstract

Silicon is a promising alternative to the conventional graphite anodes due to its high theoretical capacity and favorable lithiation potential for lithium-ion batteries (LIBs) with liquid as well as solid-state electrolytes. However, lithiation-induced extreme volume change causes severe mechanochemical deformation and continuous formation of solid-electrolyte interphase leads to cell failure. One of the strategies to mitigate this problem is alloying silicon with a suitable element that can alter the surface electrochemistry and/or lithiation pathways, and acts as mechanical buffer. Nonetheless, these benefits come with a compromise on the specific capacity, which strongly influences the mass loading of the electrodes, highlighting the need to deconvolute the intertwined influence of composition and mass loading when designing high performance electrodes. In this work, we systematically studied the influence of composition and mass loading in monolithic amorphous silicon and non-stoichiometric silicon nitride (SiN_x) electrodes on their electrochemical performance as LIB anodes. The incorporation of nitrogen in the electrode matrix clearly improves the electrochemical stability at the expense of reduced specific capacity, while higher mass loading accelerates capacity fading, most critically in amorphous silicon electrodes. Postmortem analysis reveals that such capacity fading in the electrodes with higher mass loading can be related to delamination due to evolved tensile stress during the charge–discharge cycle. Yet, nitrogen-rich SiN_x monolithic electrodes accommodate strain more effectively. These findings demonstrate that while pristine Si delivers high specific capacity and long-term stability in thin films, thicker (>1 μm) monolithic electrodes benefit from higher nitrogen content in SiN_x, which provides more stable cycling and sustained capacity.

1. Introduction

Lithium-ion batteries (LIBs) underpin modern portable electronics, electric vehicles, and stationary energy-storage systems, yet their continued advancement is increasingly constrained by the limited specific capacity of commercial graphite anodes (372 $mAh.g^{-1}$) [1]. Silicon, an alloy-able material for anode applications, has emerged as promising alternative due to its exceptionally high theoretical capacity (3579 $mAh.g^{-1}$) [2], inherently-high electronic conductivity, and favorable lithiation potential of 0.4 V vs Li^+/Li [3–5]. Not only in conventional LIBs with liquid electrolyte, but also in thin-film and solid-state batteries, silicon has exhibited promising performance enhancement [6–10]. However, reversible storage of such huge amount of lithium can result in a volume expansion up to 300% [2, 11], leading to severe mechanochemical deformation along with steady decline of lithium reservoir due to continuous formation of solid electrolyte interphase (SEI). All this hinders the scope of use of silicon as next generation, high-capacity anode material.

Such limitations of the silicon-based anodes have been addressed through nanostructuring, porosity modulation, composite preparation with graphite, or other suitable low-capacity anode materials, artificial SEI deposition, etc [12–17]. Recently, there have been reports on 100% silicon anodes, where strategic incorporation of porosity, nanostructuring and restricted cycling protocol demonstrated 100% capacity retention after 1800 cycles [18, 19]. Another approach to address electrochemical instability issues lies in alloying of silicon with other elements [20], which can be achieved through scalable vapor based deposition methods. For example, Ulvestad *et al* [13] demonstrated the incorporation of nitrogen in silicon leads to enhanced electrochemical stability over composites containing silicon microparticles. In a nutshell, the introduction of a suitable foreign element not only stabilizes the surface electrochemistry, but also acts as an active buffer by limiting the amount of accessible specific capacity [21–23]. Such mechanochemical characteristics make these materials promising for not only thin-film anodes, but also high-capacity anodes. Implementing such materials as monolithic anodes eliminates the need for additives along with solvent-based composite processing, and provides higher volumetric energy density compared to composite electrodes, making them attractive for high-performance LIBs [13, 24, 25].

However, this benefit of introducing a buffering matrix in silicon-based electrodes is always accompanied by a compromise in the specific capacity values, which sharply decline with increased electrode mass loading. Such trade-off was highlighted by Ulvestad *et al* and demonstrated by studying the reversible capacity of silicon nitride nanoparticles as a function of stoichiometry [13]. Since the electrochemical performance of an electrode is directly correlated with the effective ionic and electronic conductivities of the material, the composition of buffering matrix plays a crucial role in defining the advantage of alloy based anodes over their pristine counterpart. For example, Kilian *et al* reported the formation of lithium nitride (Li_3N) in the buffering matrix which improved the lithium-ion transport kinetics in the matrix of LIB anodes containing non-stoichiometric silicon nitride nanoparticles (SiN_x-NP) [26]. However, in these studies the use of SiN_x-NP implies the use of high temperature processes for nanoparticle synthesis followed by solvent-based slurry coating. This results in anodes either with low mass-loadings or with reduced energy density due to added binders and additives. Monolithic films can address some of these drawbacks but the impact of increased mass-loading is rarely addressed. For instance, Lee *et al* report a 95.4% capacity retention for sputtered SiN0.85 monolithic films after 100 cycles, yet anode thickness remains low, at approximately 200 nm [27]. Therefore, for an optimized design of such electrodes for high performance LIBs, it is essential to investigate the intertwined influence of alloy composition and film morphology on their electrochemical behavior.

To study this, we first deposited monolithic films of amorphous silicon and non-stoichiometric silicon nitride, systematically tuning the nitrogen content ($SiN_{0.2}$, $SiN_{0.4}$ and $SiN_{0.6}$) and mass loadings by varying the deposition time (0.5, 1 and 1.5 h) using plasma enhanced chemical vapor deposition (PECVD). Then, we compared the rate performance as well as long-term cyclability of these films as LIB anode. The development of these monolithic electrodes provides a unique opportunity to deconvolute the influence of composition, mass-loading as well as morphology modulation on battery performance. Finally, to relate the electrode composition and structure to electrochemical performance, we conducted post-mortem investigation on amorphous silicon and sub-stoichiometric amorphous silicon-nitride that shine light on the microscale degradation mechanisms occurring during charge–discharge cycles.

2. Methods

2.1. Electrode deposition

Hydrogenated amorphous silicon and silicon nitride films (a-Si:H and a-SiN_x:H, hereafter referred to as Si and SiN_x, respectively) were deposited using PECVD method on 12 μm thick textured copper foil (Civens®, figure S1) for electrochemical testing and physical characterization. Substrate temperature, chamber pressure and RF power density were kept at 180 °C, 0.8 mbar and 75 ± 2 mW·cm^{-2}, respectively. For all a-SiN_x:H depositions, total precursor gas-flow rate (ϕ_T) was kept at 50 sccm, except for a-Si:H deposition for which ϕ_T was set to 40 sccm. Film composition was adjusted by varying the gas-flow-rate ratio R, defined as:

$$R = \frac{\phi_{NH_3}}{\phi_{NH_3} + \phi_{SiH_4}}$$

where ϕ_{NH_3} and ϕ_{SiH_4} are the ammonia and silane gas-flow rates, respectively. In this work, R is varied from 0 to 0.85, within a 4% relative error. For any given flow-rate ratio, samples were deposited for 0.5, 1.0, and 1.5 h with under 30 s variation, attributed to plasma ignition time. Mass loading was determined by weighing the copper substrates before and after film deposition using a precision weighing scale (VWR® 611-3800, precision: ±0.01 mg).

2.2. Material characterization

Film morphology and roughness were assessed by atomic force microscopy (AFM, Bruker Dimension FastScan) in tapping mode and analyzed using Gwyddion. Scanning electron microscopy (Hitachi Regulus SEM, 1 kV) was used to evaluate surface and cross-sectional morphology and inspect anodes post-mortem. Raman spectroscopy (Renishaw InVia Microscope, 514 nm excitation) confirmed film micro-structure and bonding environments. X-ray photoelectron spectroscopy was carried out in a Physical Electronics (PHI) 5400 (Eden Prairie, USA) instrument for binding energy in the 0–1100 eV range to provide elemental composition and bonding states. Measurements were carried out after 20 min long surface sputtering by argon to minimize the impact of surface oxidation on the measurement. The XPS spectra were acquired by using non-monochromatic Al K*a* radiation produced from an x-ray source with an Al anode, operating at 200 W and 13.5 kV. The primary photoelectron lines for each element were captured with a step size of 0.2 eV, employing a spherical capacitor analyzer configured with a pass energy of 71.55 eV and 89.45 eV for high resolution and survey spectra, respectively. Energy-dispersive x-ray spectroscopy (FEI NovaNano SEM with EDX detector, 15 kV) and optical microscopy (OM) (Olympus MX63) were used for elemental mapping and surface inspection, respectively, during post-mortem analysis after opening the cells in argon atmosphere and cleaning the anode with dimethyl carbonate (DMC).

2.3. Electrochemical characterization

All electrochemical measurements were conducted in CR2032-type cells assembled in an argon-filled glovebox (MBraun Labmaster 130) with oxygen and moisture levels maintained below 2.5 ppm. The working electrodes were punched into 13 mm diameter discs (1.327 cm^2 surface area) and assembled with LP40 electrolyte ($LiPF_6$:EC:DEC in a 1:7.1:3.9 ratio with 10% w/w FEC additive), Whatman glass microfiber filter as separator and cycled in a half-cell configuration against a lithium-metal counter-electrode. All cells underwent 4 formation cycles at a C-rate of C/20 in a 0.01–1.5 V voltage window vs Li/Li^+. Rate capability tests were then performed by sequentially increasing the C-rate from C/10 to C/5 (0.05–1 V vs Li/Li^+), with each rate applied for five consecutive cycles. The C-rate was then returned to C/10 for 5 cycles as a resilience test to evaluate capacity recovery. Following these rate tests, stability was assessed by cycling the cells at C/5 for 100 cycles (0.05–1 V vs Li/Li^+). C-rate was calculated from measured mass loading and theoretical specific capacity of the material (3579 $mAh.g^{-1}$ for Si, 3628 $mAh.g^{-1}$ for SiN_x) [26]. electrochemical impedance spectroscopy (EIS) was carried out within a frequency range of 1 MHz to 100 mHz using Biologic VMP 300. Distribution of relaxation times (DRT) analysis was carried out using RelaxIS 3 software by rhd instruments.

3. Results and discussions

3.1. Physiochemical characterization of PECVD deposited Si and SiN_x electrodes

Investigating the impact of the nitrogen content in and mass loading of SiN_x films on anode performance requires reliable and consistent PECVD processing. For all samples, only deposition time, ϕ_{NH_3}, ϕ_{SiH_4} and hence the flow-rate ratio, R, were varied. Figure 1(a) shows the measured mass loading of the deposited films as a function of deposition time for flow-rate ratios R ranging from 0 to 0.85. For every deposition condition, mass loading was measured by punching out and weighing 6 discs (13 mm diameter), their weight distribution is represented as error bars in figure 1(a) and is attributed to slight non-uniformity in the film deposition. As expected, mass loading increases linearly with deposition time across all R values. Similar deposition rates were found for all, leading to films with different nitrogen content having comparable mass loadings for a given deposition time.

Cross-sectional SEM images of silicon films deposited for 0.5, 1, and 1.5 h (figures 1(b)–(d)) reveal the impact of underlying copper collector roughness (figure 1(e)) on film morphology. The conformal nature of PECVD film growth leads to bulge-like features being formed with pronounced local variations in film thickness. Those variations tend to level out for thicker films as conformal growth smoothens the surface. Although precise thickness measurement is not achievable for such samples, the 0.5, 1, and 1.5 h Si depositions (figures 1(b)–(d)) were found to have average thicknesses ∼570, 1550 and 3170 nm, respectively. AFM measurements of the copper substrate and Si depositions (figures 1(e)–(g)) confirm this trend with the thicker Si film (1 h) having a significantly lower root mean square roughness ($R = 295$ nm) than the thinner Si film (0.5 h, $R_q = 385$ nm). SiN*x* films are also expected to follow similar trend, due to their amorphous nature yielding conformal growth on textured interfaces [28].

Raman spectroscopy and x-ray photoelectron spectroscopy measurements were carried out on nitrogen containing samples (0.5 h deposition time) to characterize the microstructure, bonding environment and stoichiometry of the deposited materials. Raman spectra for SiN_x deposited at $R = 0.50$, 0.76 and

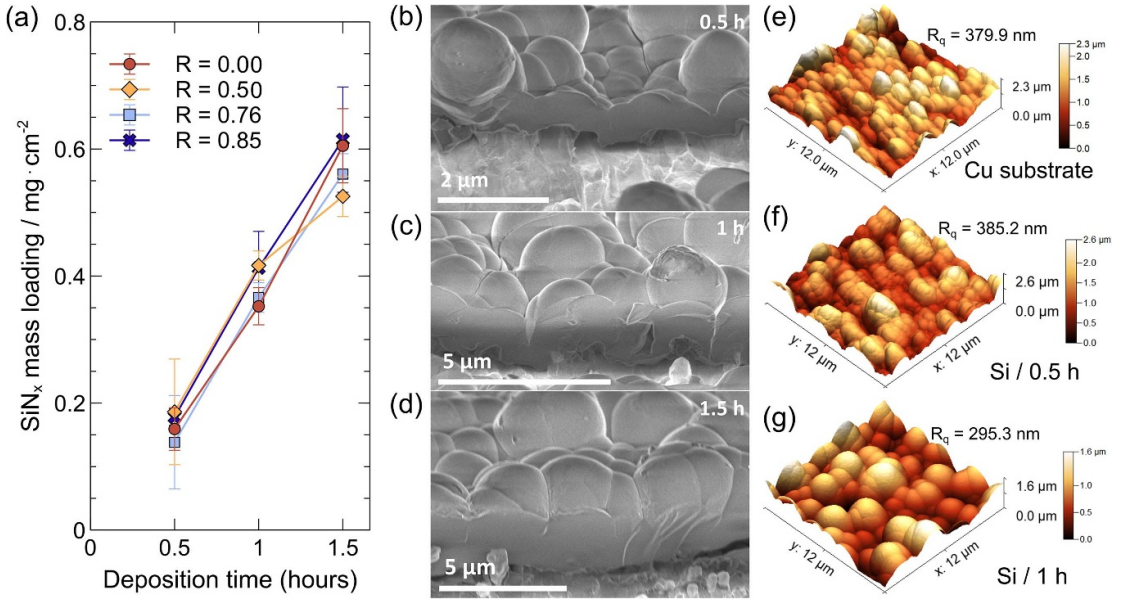

Figure 1. (a) Active material mass loading for increasing flow-rate ratios R as a function of deposition time. Cross-sectional SEM images (∼30° tilt) of Si layers deposited on rough copper foil for (b) 0.5 h, (c) 1 h and (d) 1.5 h. AFM mapping and RMS roughness (R_q) of the (e) pristine Cu current collector, (f) 0.5 h and (g) 1 h Si deposited on rough copper foil.

0.85 are displayed in figure 2(a). Each Raman spectrum was normalized with respect to the Si–Si transverse optical (TO) peak at 480 cm^{-1}. Four peaks were identified in all samples: Si–Si transverse acoustic (TA) peak at ∼165 cm^{-1}, Si–Si (TO) peak at 480 cm^{-1}, Si–H_2 wagging mode at 640 cm^{-1}, Si–N stretching peak at ∼900 cm^{-1} and finally the Si–H_n stretching modes at ∼2100 cm^{-1} [29–37]. The wide asymmetric Si–Si TO peak centered at 480 cm^{-1} found in every spectrum is indicative of the amorphous nature of the films. The increase of Si–N peak intensity with R, relative to the Si–Si TO peak, is also a qualitative marker for the increase nitrogen content as ammonia gas flow is increased. The Si–H_n peak located at higher Raman shift shows a clear relative intensity increase as well as a shift towards higher wavenumbers. Such shift can be attributed to an increase in Si–H_2 bonds with respect to Si–H bonds, indicating presence of micro-voids in the material [38, 39]. Accordingly, an increase in the relative intensity of the Si–H_n peak with respect to the Si–Si TO peak can signify presence of more porosity in the SiN_x samples with higher N-content. To our knowledge, there is still little understanding of the role of hydrogen in PECVD deposited alloy materials on their electrochemical performance [40]. The systematic study of the effects of hydrogen content and bonding configuration on cell performance was however deemed beyond the scope of this study.

Further chemical investigation was carried out using XPS. Figure 2(b) shows the high-resolution spectra for the Si 2p peak of SiN_x deposited at R = 0.50, 0.76 and 0.85. Each peak was deconvoluted into 3 Gaussian curves attributed to 3 valence states representative of Si–Si, Si–N and Si–O bonds in the film [41, 42]. Despite Ar sputtering of the surface, traces of oxygen were found in the layers indicating possible subsurface oxidation due to the microporous nature of the films seen in the Si–H Raman peak. Similarly to what has been observed with Raman spectroscopy, increasing R leads to the bonding state of Si atoms to shift from Si^0 to higher valence states [41]. Relative integrated areas of the N 1s and Si 2p peaks were used to quantitatively assess the N:Si atomic ratio of the films [24, 42]. Full range XPS survey spectra are included in figure S2.

Nitrogen content as a function of flow rate ratio is given in table 1. All deposited films were found to be sub-stoichiometric ([N]/[Si] < 1.33) with a [N]/[Si] ratio consistently lower than R indicating a preferred incorporation of silicon in the films during deposition. For better clarity, deposited electrodes will further be referred to by their respective composition, i.e. Si, $SiN_{0.2}$, $SiN_{0.4}$ and $SiN_{0.6}$.

3.2. Electrochemical performance

Si and SiN_x monolithic electrodes were assembled into coin cells and cycled in a half cell configuration against Li-metal. Electrodes mass loadings corresponding to cycled cells are given in table S1. Figure 3 displays the specific capacity values of the electrodes during rate performance tests. First, the formation cycles (cycle 1–4) were carried out at C/20 in an extended voltage window (0.01–1.5 V vs Li/Li^+)

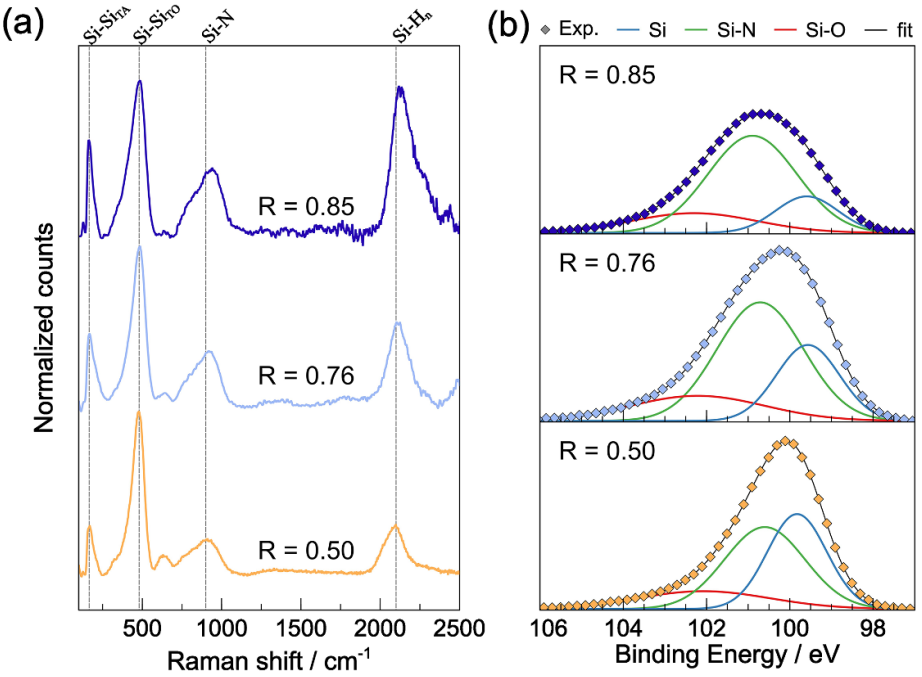

Figure 2. (a) Raman spectra and (b) XPS spectra for nitrogen containing monolithic silicon anodes deposited with increasing flow rate ratio *R*.

Table 1. Atomic nitrogen to silicon ratio as a function of flow-rate ratio *R* obtained from XPS quantitative analysis.

Flow rate ratio *R*	(N)/(Si) ratio from XPS	Electrode ID
0.00	—	Si
0.50	0.219	$SiN_{0.2}$
0.76	0.406	$SiN_{0.4}$
0.85	0.606	$SiN_{0.6}$

to ensure complete lithiation of the material (see differential capacity curves, figure S3) and promote stable SEI formation. The thinner 0.5 h deposited electrodes (figure 3(a)) show a minimal capacity loss during the formation cycles; after the formation cycles the Si, $SiN_{0.2}$, $SiN_{0.4}$ and $SiN_{0.6}$ electrodes show specific capacities of 3263, 2903, 2970 and 1712 mAh·g^{-1}, respectively, along with retention of 75.4%, 68.2%, 72.2% and 58.3% of their respective end-of-formation capacity after the rate performance tests (cycle 5–14). To evaluate the electrochemical resilience of these electrodes the cells were cycled again at C/10 after the rate performance test (cycle 15–20). Voltage profiles for the last cycle of every C-rate step are displayed in figure S4. As shown in figure 3(a), the specific capacity values were reproduced within less than 2.5% error. In terms of cell performance values, the electrodes with Si shows the highest specific capacity as well as the rate performance, followed by $SiN_{0.2}$, $SiN_{0.4}$ and $SiN_{0.6}$. The lowest specific capacity obtained for $SiN_{0.6}$ is attributed to the formation of a higher fraction of the inactive Li_2SiN_2 phase in SiN_x with increasing nitrogen content [13, 43], which was also observed by Lovett *et al* [44].

Figure 3(b) shows the rate performance of the electrodes where the active materials were deposited for 1 h. Unlike the 30 min deposited samples, these electrodes exhibit steep capacity degradation during the formation cycles. After the last formation cycle, the specific capacity values of the Si, $SiN_{0.2}$, $SiN_{0.4}$ and $SiN_{0.6}$ were found to be 3429, 2329, 2370 and 2146 mAh·g^{-1}, respectively. At the end of the rate performance tests, the Si, $SiN_{0.2}$, $SiN_{0.4}$ and $SiN_{0.6}$ electrodes retained 35.4%, 20.7%, 62.1% and 41.7% of their end-of-formation capacity values. Note, before the rate performance test, the coulombic efficiency of these cells (figure S5) can be as low as 87.2%, 83.2%, 95.8%, 93.6%. However, during the resilience test the average coulombic efficiency values are stabilized at 97.3%, 99.5%, 99.2% and 99.6% for Si, $SiN_{0.2}$, $SiN_{0.4}$ and $SiN_{0.6}$ electrodes, respectively (see figure S6).

The rate performance of the 1.5 h deposited samples are shown in figure 3(c). During the formation cycles, all electrodes show significant capacity fading, except the $SiN_{0.6}$ electrode. After the formations cycles the capacity of the Si, $SiN_{0.2}$, $SiN_{0.4}$ and $SiN_{0.6}$ electrodes were 2528, 1799, 2227 and

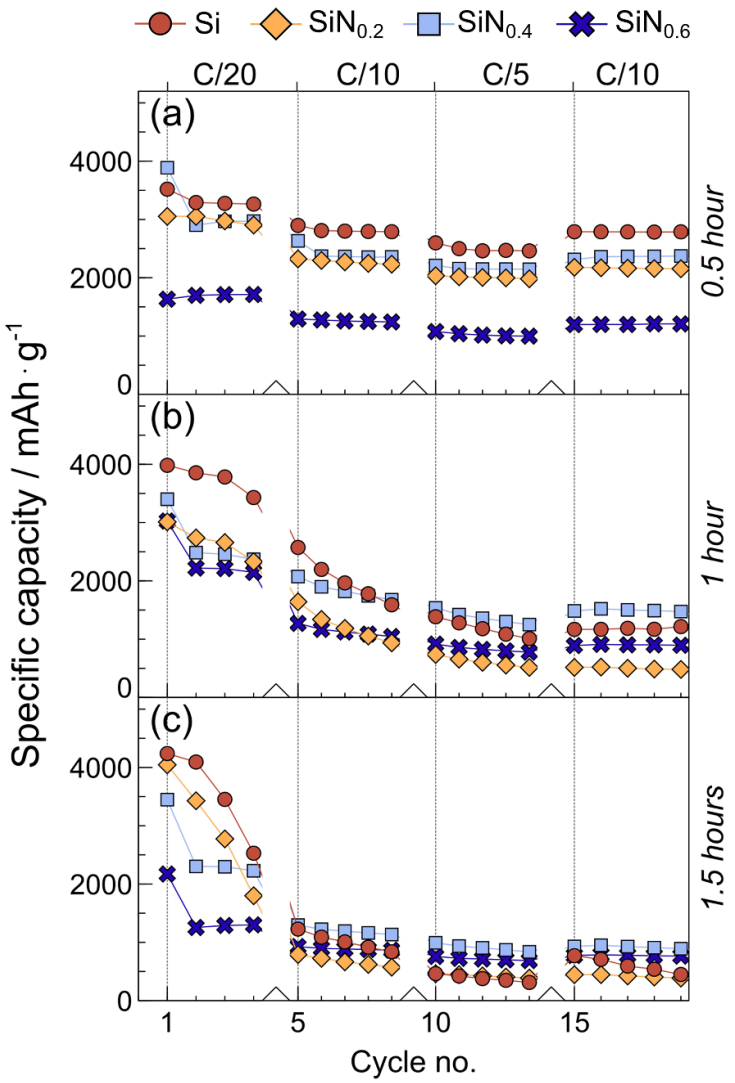

Figure 3. Specific (discharge) capacity during formation cycles (4 × C/20) and rate testing (5 × C/10, 5 × C/5, 5 × C/10) for Si and SiN*x* anodes with increasing nitrogen content. For each nitrogen content films were deposited at increasing deposition time corresponding to (a) low mass loading (tdep = 0.5 h, $\overline{m}_{anode} \sim 0.16$ mg·cm^{-2}), (b) intermediate mass loading (tdep = 1 h, $\overline{m}_{anode} \sim 0.39$ mg·cm^{-2}) and (c) high mass loading (tdep = 1.5 h, $\overline{m}_{anode} \sim 0.58$ mg·cm^{-2}). Across all compositions, increase in deposition time leads to capacity degradation with Si and SiN0.2 exhibiting unstable formation for tdep of 1 and 1.5 h.

1300 mAh·g^{-1}, respectively, and retained 12.3%, 21.5%, 37.5%, 52.8% of their end-of-formation capacity at the end of the rate performance tests. Unlike 0.5 h and 1 h deposited electrodes, the 1.5 h deposited electrodes kept showing declining capacity trend even during the stability test.

From the results of the rate capability tests, followed by the resilience tests, two clear conclusions can be drawn. First, with increasing N-content, the specific capacity values of the SiN_x electrodes decrease while gaining in capacity retention. As previously reported by Kilian *et al* [26], during the first few lithiation and delithiation cycles, the SiN_x electrode transforms into a matrix combining amorphous Si with $LiSiN_x$ and LiN_x. Considering the $LiSiN_x$ and LiN_x contribute to enhanced lithium-ion kinetics and a buffering effect in the electrode, an increasing content of such buffering matrix would lead to better mechanochemical stability against the volume change during the lithiation and delithiation cycles. On the other hand, a reduced content of Si in the N-rich electrodes results in lower specific capacity values. Second, with increasing materials' deposition time, the degradation in the electrochemical performance of the electrodes accelerates significantly. Such degradation in electrochemical performance is highest for the Si electrodes and lowest for the $SiN_{0.6}$. Additionally, at a given C-rate, the specific capacity of N-rich SiNx electrodes experience a sharp decline with enhanced deposition time. This trend can be attributed to the higher fraction of high bandgap lithium nitride formed within the electrode matrix, which substantially increases the electrode resistance and limits the accessible lithium-storage capacity in thicker electrodes.

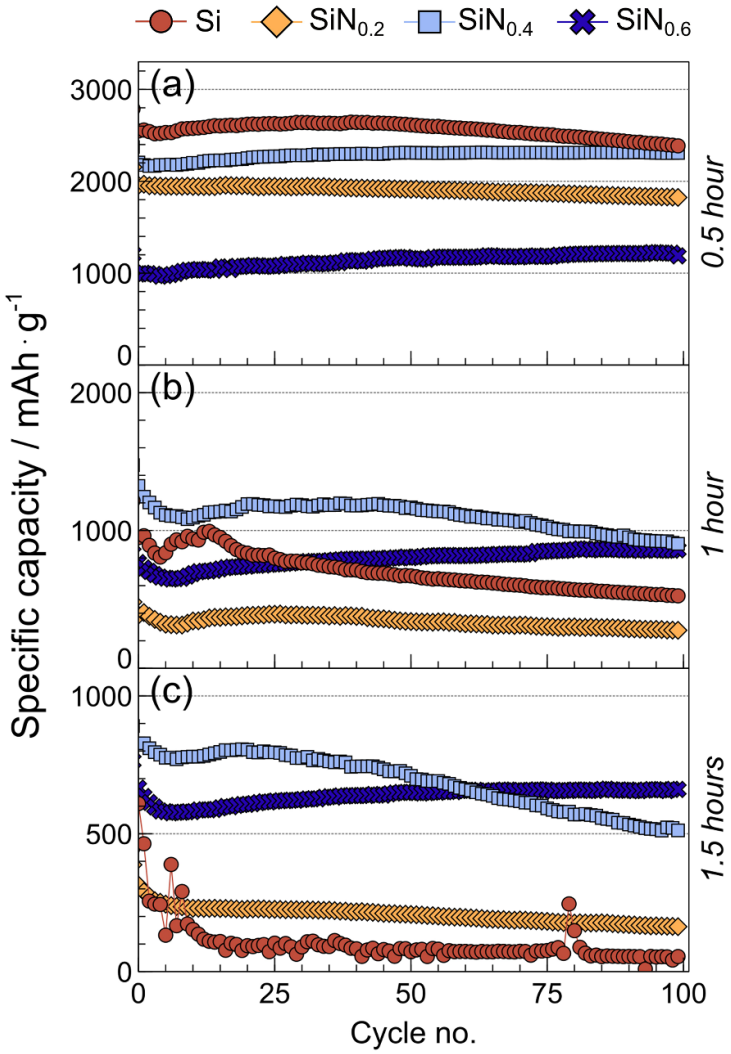

Figure 4. Influence of nitrogen composition and active material mass loading on anode specific (discharge) capacity and cycling stability. Cells were cycled at C/5 for 100 cycles following rate testing (see figure 3). Increasing deposition time—(a) 0.5 h, (b) 1 h and (c) 1.5 h leads to increasing mass loading. At low mass loading silicon outperforms SiN_x alloys both in specific capacity and stability but the trend quickly reverses at higher mass loading, with the N-rich $SiN_{0.6}$ alloy reaching a stable capacity of 661 $mAh{\cdot}g^{-1}$ after 100 cycles with a areal capacity of 0.486 $mAh.cm^{-2}$.

Long-term capacity retention of these materials was then assessed by cycling these cells for 100 cycles at C/5. Figures 4(a)–(c) display the specific capacity obtained across all anode deposition times (4a- 0.5 h, 4b- 1 h and 4c- 1.5 h) for every Si and SiN_x electrodes with different nitrogen content. Corresponding coulombic efficiency values can be found in the supplementary materials figure S6, with representative voltage profiles in figure S7. Both Si and $SiN_{0.2}$ are found to maintain high capacity after 100 cycles for low deposition time (30 min, m_{anode} = 0.177 $mg.cm^{-2}$ and 0.168 $mgcm^{-2}$, respectively). For the same materials, 1 h deposited electrodes start showing important capacity loss and 1.5 h depositions rapidly lead to complete cell failure. Unlike aforementioned Si and $SiN_{0.2}$, $SiN_{0.4}$ and $SiN_{0.6}$ electrodes experience a specific capacity increase for low mass loadings (m_{anode} = 0.140 $mg.cm^{-2}$ and 0.187 $mg.cm^{-2}$, respectively). $SiN_{0.6}$ still exhibits this behavior even for higher mass loadings, whereas $SiN_{0.4}$ moves to a capacity degradation trend analogous to $SiN_{0.2}$, albeit notably outperforming the latter. This slow performance improvement during cycling is seen in $SiN_{0.4}$, $SiN_{0.6}$, and to some extent in the initial cycles of 0.5 h Si (figure 4(a)). This effect can be attributed to formation of increasing amounts of Li_3N and Li_2SiN_2 over time, allowing for better Li^+ ion conductivity and enhanced lithiation [13] as the SEI stabilizes and slowly converts to these compounds. This mechanism enables SiN_x with high nitrogen content to reach better electrochemical performance, with $SiN_{0.6}$ attaining specific capacities of 661 $mAh.g^{-1}$ after formation, rate-testing and 100 cycles at C/5 for a 0.735 $mg{\cdot}cm^{-2}$ mass loading.

To correlate the long-term capacity retention of these electrodes with their composition and mass loading, the capacity retention after 100 cycles at C/5 is displayed as a function of N/Si ratio and active material mass loading in figure 5. For every cell, capacity retention was calculated from the ratio of

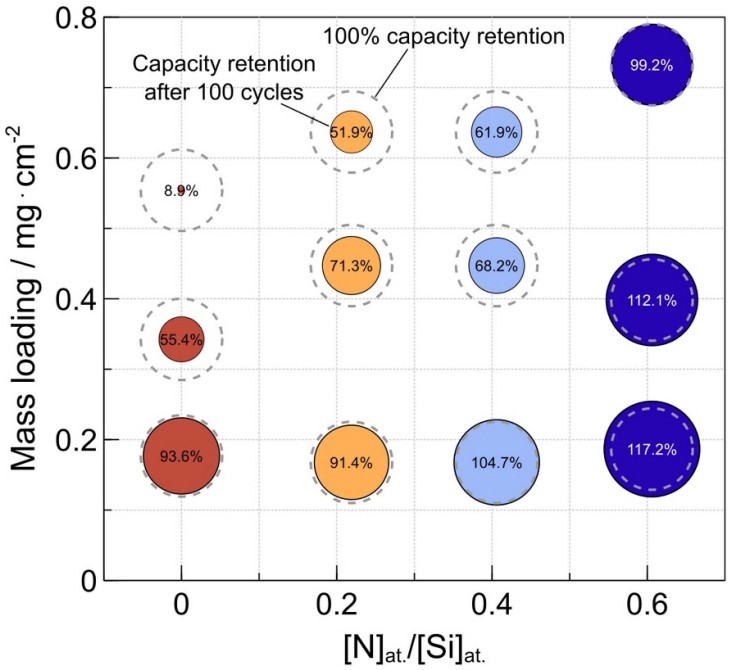

Figure 5. Capacity retention as a function of mass loading and nitrogen content of Si and SiN_x. Capacity retention was calculated based on the specific capacity ratio between the 100th cycle and 1st cycle at C/5 during long term testing (see figure 4). Capacity retention is represented by dot diameter, with the gray dashed circle representing 100% capacity retention. Capacity retention above 100% indicates the material has a higher specific capacity after 100 charge–discharge cycles.

the specific capacity measured after the 100th cycle vs the 1st cycle of stability testing (see figure 4). A clear trend emerges from the tested materials, with the capacity retention for Si plummeting from 93.6% to 8.9% for an increase in mass loading from 0.178 to 0.554 mg.cm^{-2}. At the other end of spectrum, sub-stoichiometric $SiN_{0.6}$ alloy reaches lower specific capacity across the tested mass loading range, yet it delivers that capacity consistently with a 117.2% capacity retention only fading to 99.2% as mass loading is increased from 0.187 to 0.732 mg.cm^{-2}. Capacity retention exceeding 100% underlines the gradual specific capacity increase seen in figure 4. As previously discussed, it is thought to be a consequence of increased Li^+ conductivity in the electrode matrix [43, 45].

In $SiN_{0.6}$, this effect outweighs the common degradation mechanisms hindering battery performance in silicon-based anodes, such as cracking, pulverization and excess SEI formation. Herein, the presence of a lithium conducting buffering matrix helps in the retaining a steady specific capacity during extensive cycling process. For reference, nanoparticle-based SiN_x anodes sustaining specific capacities in the 1000 mAh.g^{-1} range after up to 1000 cycles have been reported elsewhere [13, 26, 46]. However, the use of binders and additives such as carbon black come at the cost of decreased volumetric density. On the other hand, SiN_x processed as a monolithic material in a thin-film configuration has also been reported to reach stable specific capacities above 1200 mAh.g^{-1} for up to 2000 cycles for a film thickness under 160 nm [47, 48], which must be compared to the 3 μm thickest anodes reported here.

Anodes with intermediate nitrogen content yield similar capacity retention as mass loading increases. Despite $SiN_{0.4}$ not clearly out-performing $SiN_{0.2}$ in terms of capacity retention only, a closer look at their respective specific capacity after cycling (512 and 163 mAh·g^{-1}, respectively, for higher mass loadings) gives a clear advantage to $SiN_{0.4}$. The low specific capacity of $SiN_{0.2}$ could partly be a consequence of delamination during unstable formation cycles seen in figure 3 and thus cannot solely be attributed to a lesser Li^+ storage capacity of the material.

To investigate the influence of nitrogen content in the Si-based matrix on lithium transport within the monolithic structure, EIS was performed on the 1.5 h deposited electrodes, which exhibit the highest mass loading in the sample series. EIS measurements were carried out after the formation cycle, rate-performance tests, and long-term cycling (figure S8), and the data were further analyzed using the DRT method (figure S9) to compare lithium-ion transport kinetics. The relaxation processes at $\tau < 0.3$ s are attributed to resistances associated with the SEI layer and charge-transfer reactions, whereas the broad low-frequency feature at $\tau \approx 1$–30 s corresponds to solid-state lithium diffusion within the monolithic electrode. The diffusion resistance contribution, quantified as the area under this peak

($R_{\text{diff}} = \int_{\tau_1}^{\tau_2} \gamma(\tau)\, \mathrm{d}\ln\tau$), provides a direct measure of lithium diffusion in these electrodes. For the Si and $SiN_{0.2}$ electrodes, R_{diff} increases with cycling, indicating progressively hindered lithium diffusion, whereas the $SiN_{0.4}$ electrode exhibits an initial decrease in R_{diff} after the rate-performance test, followed by a significant increase after long-term cycling. In contrast, the $SiN_{0.6}$ electrode shows a continuous decrease in R_{diff} upon cycling, further supporting its enhanced lithium transport and superior capacity retention during prolonged cycling compared to the other materials.

3.3. Post-mortem investigation

To identify the failure mechanisms underlying the observed electrochemical trends, post-mortem analysis was conducted on Si and $SiN_{0.6}$ anodes after cycling. Samples with short (0.5 h), intermediate (1 h) and long (1.5 h) deposition times were selected to represent low and high mass-loading regimes, respectively. Coin cells were opened and anodes cleaned with DMC, and dried in argon atmosphere to conduct post-mortem analysis. Figure 6 gathers morphological degradation and compositional distribution data from OM, SEM, and EDX. EDX elemental mapping image is displayed for silicon only. Complete mapping results are given in figure S10(a) and (b) along with surface average EDX spectra.

For the low mass-loading (0.5 h) samples, both Si (figure 6(a)) and $SiN_{0.6}$ (figure 6(d)) anodes exhibited good adhesion to the copper current collector, with no evidence of macroscopic delamination. Closer inspection through SEM imaging revealed the formation of discrete 'islands' of active material, separated by a network of cracks. The gap between the islands was found to be in the range of 1–2 μm. The similarity in crack morphology between the two compositions suggests that mechanical stress induced by volume expansion during lithiation is a common degradation pathway. Crack presence leads to increased anode/electrolyte interface and increased lithium consumption during SEI formation. The absence of delamination indicates that the mechanical integrity of the interface is preserved at low mass loadings despite crack formation. This observation is consistent with the stable cycling performance observed in figure 4.

In contrast, intermediate (1 h) and high (1.5 h) mass loading Si anodes (figures 6(b) and (c)) suffered extensive delamination, with large regions of active material visibly detached from the substrate as identified in OM images (figures 6(b) and (c)) and in low magnification SEM-EDX maps (see figure S10(c)). Non-delaminated areas identified through SEM show residual Si 'islands' were sparsely distributed and separated by large cracks, indicating severe loss of electrochemically active material. The gap between the islands was estimated to be in the range of 3–6 μm for 1.5 h Si. This correlates with the rapid capacity fade and poor retention seen in figures 4 and 5, confirming that delamination is a dominant failure mode in thick Si films. The increased chemo-mechanical stress during formation and cycling, exacerbated by the large volume expansion of Si [49], likely exceeds the adhesion strength at the film-substrate interface.

Conversely, intermediate (1 h) and high (1.5 h) mass-loading $SiN_{0.6}$ sample (see figures 6(e)–(f)) maintained excellent adhesion, with no observable macro-scale delamination from top view OM images. The SEM and EDX analyses revealed large $SiN_{0.6}$ 'islands' and a network of thinner cracks compared to the Si equivalent. The gaps between the islands were in the range of 2.5–4.5 μm for 1.5 h $SiN_{0.6}$. Unlike the Si electrodes, the smooth material filling the cracks was identified to be SEI which is being investigated in another study by the authors. This morphological stability supports the superior capacity retention reported for $SiN_{0.6}$ in figure 5. The enhanced mechanical robustness of SiN_x films, attributed to their lower expansion coefficient [27] and improved stress accommodation through Li_2SiN_2/Li_3N buffer matrix [26, 45], mitigates delamination even at high mass loading despite the formation of an anode-wide crack network.

The formation of such a network of cracks is expected in monolithic Si-based anodes as material porosity alone cannot buffer the extreme volume change during cycling. Figure 6(g) provides a qualitative interpretation as to how the quasi-2D nature of the deposited film (a few microns in thickness vs centimeter-scale width) promotes expansion in the direction of least mechanical resistance, i.e. normal to the substrate. Upon delithiation, material retraction leads to tensile stress. If these constraints exceed material resistance cracks can start forming, allowing for volume change to occur along the x- and y-axis as well as in the normal (z) direction [50, 51]. This leads to the formation of a crack network whose nature will strongly depend on anode material and thickness. Previous study by Lovett *et al* [44] on the structural evolution of monolithic silicon nitride anodes thoroughly investigated the formation of particulate silicon domains at the nanoscale. However, these experiments are typically carried out on extremely thin films, with mass loadings almost two orders of magnitude lower than this study and are thus not designed to capture the impact of crack formation and delamination on anode performance. As such, this post-mortem study of anodes with mass loadings in the 0.15–0.74 mg·cm^{-2} range refines our

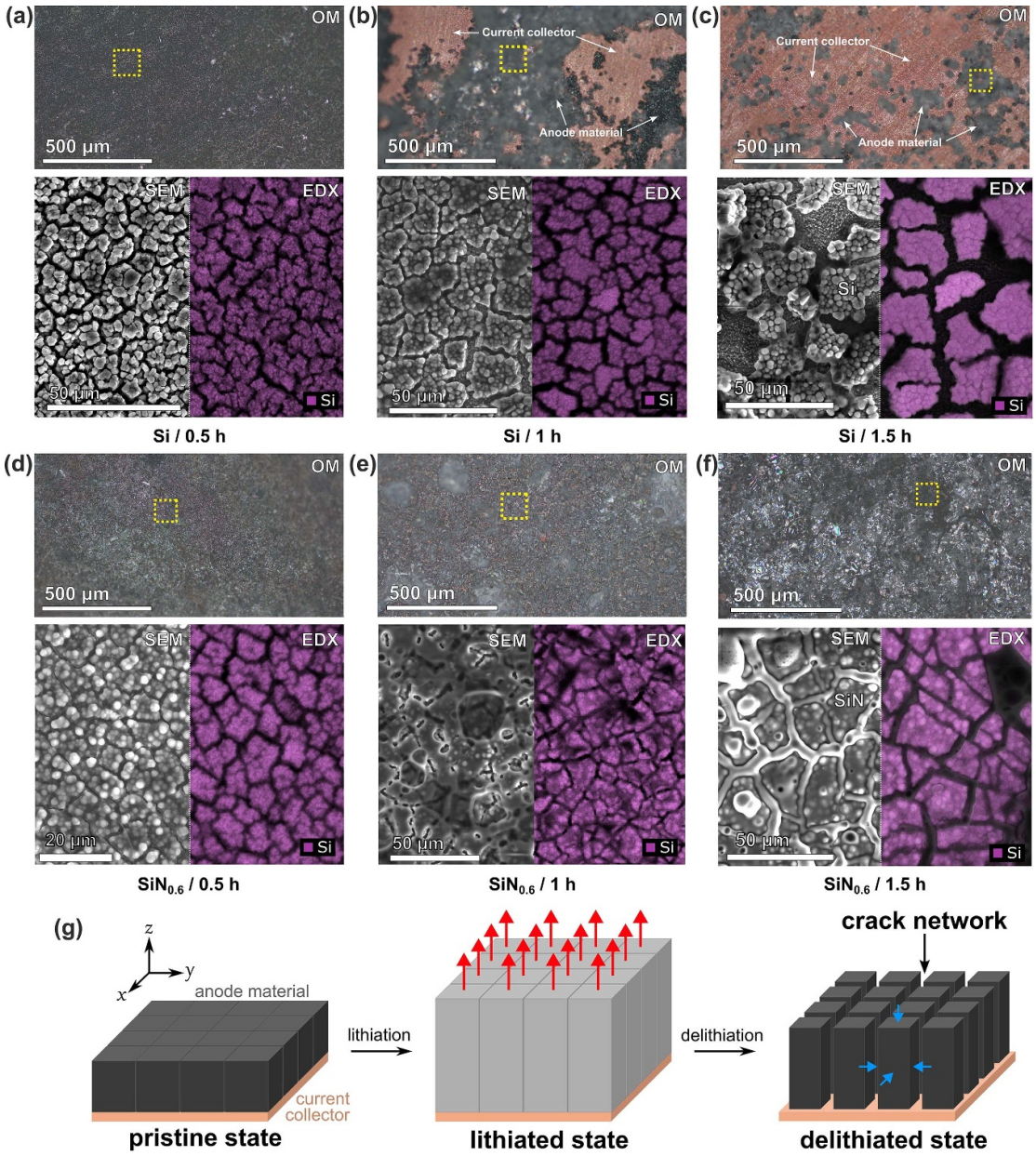

Figure 6. Post-mortem inspection (top-view) of anode material after 100 cycles at C/5. Optical microscope (OM), SEM and SEM-EDX were used for general inspection, microstructure investigation and compositional mapping (magenta indicates presence of Si), respectively. The yellow dashed square in the OM image represent the equivalent area probed by SEM and EDX. (a) 0.5 h silicon and (d) 0.5 h $SiN_{0.6}$ show no delamination from the copper current collector and exhibit similar crack formation between Si and $SiN_{0.6}$ 'islands', respectively. (b) 1 h silicon and (c) 1.5 h silicon suffered severe delamination. For 1.5 h silicon (c) non-delaminated areas show large, sparsely spread out Si 'islands' while (e) 1 h $SiN_{0.6}$ and (f) 1.5 h $SiN_{0.6}$ had no noticeable macro-scale delamination and densely packed $SiN_{0.6}$ 'islands'. (g) Schematic representation of crack formation in thin film Si-based anodes due to *z*-axis limited volume expansion during first lithiation followed by isotropic volume contraction.

understanding of electrochemical data and reinforces the conclusion that nitrogen-rich SiN_x compositions offer significant advantages in mechanical stability and long-term performance, particularly under high mass-loading conditions.

4. Conclusion

This work systematically investigates the coupled influence of nitrogen content and mass loading on the electrochemical behavior and failure mechanisms of monolithic amorphous silicon and amorphous silicon nitride anodes for LIBs. Using PECVD to precisely vary the Si:N ratio and film thickness, we demonstrate that sub-stoichiometric SiN_x compositions significantly enhance mechanical stability and cycling performance compared to amorphous silicon, particularly under high mass-loading conditions where conventional Si anodes typically fail [52].

Electrochemical analysis shows that monolithic Si electrodes exhibit high initial capacities at low mass loadings but undergoes rapid capacity decay attributed to extensive delamination with increasing mass loading. Despite underperforming at low mass loading, nitrogen-rich alloys such as $SiN_{0.6}$ maintain structural integrity and display stable cycling at high mass loading, achieving over 100% capacity retention after 100 cycles at C/5. This exceptional stability is attributed to the gradual formation of Li_3N and Li_2SiN_2 phases and subsequent improvement of Li^+ transport pathways, thus contributing to additional reversible capacity. The monolithic nature of the film also achieves an areal capacity of 0.486 mAh·cm^{-2} for an electrode thickness in the order of 3*–4 μm. To put this into perspective, similar composite anodes containing 60 wt.% $SiN_{0.69}$ microparticle reached areal capacity in a similar range (0.32–0.47 mAh·cm^{-2} at C/2) for an electrode thickness in the 5–7 μm range [13]. The subsequent improvement in volumetric energy density is largely attributed to the monolithic approach to material deposition enabled by PECVD.

Post-mortem analysis through SEM and EDX on the cycled electrodes confirms delamination and crack formation are dominant degradation mechanisms in monolithic electrodes, yet nitrogen incorporation effectively mitigates delamination by reducing volumetric strain. Nitrogen-rich SiN_x electrodes thus retain a monolithic structure, accommodating stress without loss of electrical contact due to the presence of a buffering matrix.

Our findings establish a direct link between composition-dependent stress accommodation and long-term electrochemical stability in SiN_x monolithic electrodes. Sub-stoichiometric silicon nitride emerges as a robust and scalable alternative to silicon when it comes to improving mass loading in monolithic LIB anodes, combining mechanical resilience with stable capacity retention. Our findings establish that for thin monolithic electrodes, pristine silicon wins the race of long term stability with high specific capacity, however with increased electrode thickness (over a micron), the high content of N in the SiN_x offers a more stable long-term cycling profile with high capacity. These insights provide a foundation for optimizing monolithic anode architectures for high-rate and long-life lithium-ion battery applications.

Acknowledgment

The authors thank Professor Marnix Wagemaker, of the research group Storage of Electrochemical Energy at Delft University of Technology for access to battery processing facilities.

Data availability statement

All data that support the findings of this study are included within the article (and any supplementary files).

Supporting Information available at https://doi.org/10.1088/2515-7655/ae4a4b/data1.

Author contributions

Alestair Wilson 0000-0002-0326-6109
Data curation (lead), Formal analysis (lead), Writing – original draft (lead), Writing – review & editing (lead)

Thomas A McKnelly
Data curation (lead), Formal analysis (lead)

Moumita Rana 0000-0002-9348-4491
Conceptualization (lead), Data curation (lead), Formal analysis (lead), Funding acquisition (lead), Investigation (lead), Project administration (lead), Supervision (lead), Validation (lead), Visualization (lead), Writing – original draft (lead), Writing – review & editing (lead)

References

[1] Zhao H, Li J, Zhao Q, Huang X, Jia S, Ma J and Ren Y 2024 Si-based anodes: advances and challenges in Li-ion batteries for enhanced stability *Electrochem. Energy Rev.* **7** 11
[2] Franco Gonzalez A, Yang N-H and Liu R-S 2017 Silicon anode design for lithium-ion batteries: progress and perspectives *J. Phys. Chem. C* **121** 27775–87
[3] Kang K, Lee H-S, Han D-W, Kim G-S, Lee D, Lee G, Kang Y-M and Jo M-H 2010 Maximum Li storage in Si nanowires for the high capacity three-dimensional Li-ion battery *Appl. Phys. Lett.* **96** 053110
[4] Sun L, Liu Y, Wang L and Jin Z 2024 Advances and future prospects of micro-silicon anodes for high-energy-density lithium-ion batteries: a comprehensive review *Adv. Funct. Mater.* **34** 2403032

[5] Eshetu G G, Zhang H, Judez X, Adenusi H, Armand M, Passerini S and Figgemeier E 2021 Production of high-energy Li-ion batteries comprising silicon-containing anodes and insertion-type cathodes *Nat. Commun.* **12** 5459
[6] Sakabe J, Ohta N, Ohnishi T, Mitsuishi K and Takada K 2018 Porous amorphous silicon film anodes for high-capacity and stable all-solid-state lithium batteries *Commun. Chem.* **1** 24
[7] Rana M, Rudel Y, Heuer P, Schlautmann E, Rosenbach C, Ali M Y, Wiggers H, Bielefeld A and Zeier W G 2023 Toward achieving high areal capacity in silicon-based solid-state battery anodes: what influences the rate-performance? *ACS Energy Lett.* **8** 3196–203
[8] Lewis J A, Cavallaro K A, Liu Y and McDowell M T 2022 The promise of alloy anodes for solid-state batteries *Joule* **6** 1418–30
[9] Xia Q *et al* 2023 All-solid-state thin film lithium/lithium-ion microbatteries for powering the internet of things *Adv. Mater.* **35** 2200538
[10] Cheng Y-W, Chen C-H, Wang S-A, Li Y-C, Peng B-L, Huang J-H and Liu C-P 2022 Propelling performance of silicon thin film lithium ion battery by appropriate dopants *Nano Energy* **102** 107688
[11] Zhu J, Wang T, Fan F, Mei L and Lu B 2016 Atomic-scale control of silicon expansion space as ultrastable battery anodes *ACS Nano* **10** 8243–51
[12] McBrayer J D *et al* 2021 Calendar aging of silicon-containing batteries *Nat. Energy* **6** 866–72
[13] Ulvestad A, Skare M O, Foss C E, Krogsæter H, Reichstein J F, Preston T J, Mæhlen J P, Andersen H F and Koposov A Y 2021 Stoichiometry-controlled reversible lithiation capacity in nanostructured silicon nitrides enabled by *in situ* conversion reaction *ACS Nano* **15** 16777–87
[14] Je M, Han D-Y, Ryu J and Park S 2023 Constructing pure Si anodes for advanced lithium batteries *Acc. Chem. Res.* **56** 2213–24
[15] Salah M, Hall C, Yap P L and Fabretto M 2024 Silicon-tin thin-film anodes for low and high power-density lithium-ion batteries *Thin Solid Films* **796** 140332
[16] Kondracki Ł, Niemelä J-P, Baster D, El Kazzi M, Utke I and Trabesinger S 2024 Synergy of artificial SEI and electrolyte additive for improved performance of silicon electrodes in Li-Ion batteries *ACS Appl. Energy Mater.* **7** 9336–48
[17] Reyes Jiménez A, Klöpsch R, Wagner R, Rodehorst U C, Kolek M, Nölle R, Winter M and Placke T 2017 A step toward high-energy silicon-based thin film lithium ion batteries *ACS Nano* **11** 4731–44
[18] Rana M, Pendashteh A, Schäufele R S, Gispert J and Vilatela J J 2022 Eliminating solvents and polymers in high-performance Si anodes by gas-phase assembly of nanowire fabrics *Adv. Energy Mater.* **12** 2103469
[19] Pendashteh A, Tomey R and Vilatela J J 2024 Nanotextile 100% Si anodes for the next generation energy-dense Li-ion batteries *Adv. Energy Mater.* **14** 2304018
[20] Zeman M, Isabella O and Swaaij R A C M M V 2024 Anode based on hydrogenated amorphous silicon carbide for application in lithium-ion batteries
[21] Nandan R, Takamori N, Higashimine K, Badam R and Matsumi N 2022 Zinc blende inspired rational design of a β-SiC based resilient anode material for lithium-ion batteries *J. Mater. Chem. A* **10** 5230–43
[22] Du J, Zhu R, Chen Q, Xie J, Xian H, Zhang J and Zhu J 2023 *In situ* synthesis of stable silicon carbide-reinforced silicon nanosheets from organoclay for high-performance lithium-ion battery anodes *Appl. Surf. Sci.* **617** 156566
[23] Gautam M, Mishra G K, Furquan M, Bhawana K, Kumar D and Mitra S 2023 Design of low-stress robust silicon and silicon-carbide anode with high areal capacity and high energy density for next-generation lithium-ion batteries *Chem. Eng. J.* **472** 144916
[24] Zhang Y, Tang W, Gao H, Li M, Wan H, Kong X, Liu X, Chen G and Chen Z 2024 Monolithic layered silicon composed of a crystalline–amorphous network for sustainable lithium-ion battery anodes *ACS Nano* **18** 15671–80
[25] Wu Y, Huang X, Huang L, Guo X, Ren R, Liu D, Qu D and Chen J 2018 Self-healing liquid metal and Si composite as a high-performance anode for lithium-ion batteries *ACS Appl. Energy Mater.* **1** 1395–9
[26] Kilian S O, Wankmiller B, Sybrecht A M, Twellmann J, Hansen M R and Wiggers H 2022 Active buffer matrix in nanoparticle-based silicon-rich silicon nitride anodes enables high stability and fast charging of lithium-ion batteries *Adv. Mater. Interfaces* **9** 2201389
[27] Lee H, Kim K-B and Choi J-W 2020 Transparent SiN thin-film anode for thin-film batteries by reactive sputtering at room temperature *Chem. Eng. J.* **401** 126086
[28] Ingenito A, Luxembourg S L, Spinelli P, Liu J, Ortiz Lizcano J C, Weeber A W, Isabella O and Zeman M 2016 Optimized metal-free back reflectors for high-efficiency open rear c-Si solar cells *IEEE J. Photovolt.* **6** 34–40
[29] Marinov M and Zotov N 1997 Model investigation of the Raman spectra of amorphous silicon *Phys. Rev. B* **55** 2938–44
[30] Beshkov G, Lei S, Lazarova V, Nedev N and Georgiev S S 2002 IR and Raman absorption spectroscopic studies of APCVD, LPCVD and PECVD thin SiN films *Vacuum* **69** 301–5
[31] Wada N, Solin S A, Wong J and Prochazka S 1981 Raman and IR absorption spectroscopic studies on α, β, and amorphous Si3N4 *J. Non-Cryst. Solids* **43** 7–15
[32] Johnson E V, Kroely L and Roca I Cabarrocas P 2009 Raman scattering analysis of SiH bond stretching modes in hydrogenated microcrystalline silicon for use in thin-film photovoltaics *Sol. Energy Mater. Sol. Cells* **93** 1904–6
[33] Lucovsky G, Nemanich R J and Knights J C 1979 Structural interpretation of the vibrational spectra of a -Si: h alloys *Phys. Rev. B* **19** 2064–73
[34] Vogelgesang R, Grimsditch M and Wallace J S 2002 Polarized ultraviolet Raman spectroscopy of β-Si3N4 *J. Appl. Phys.* **92** 3103–6
[35] Bandet J, Despax B and Caumont M 1999 Nitrogen bonding environments and local order in hydrogenated amorphous silicon nitride films studied by Raman spectroscopy *J. Appl. Phys.* **85** 7899–904
[36] Fischer B, Lambertz A, Nuys M, Beyer W, Duan W, Bittkau K, Ding K and Rau U 2023 Insights into the Si─H bonding configuration at the amorphous/crystalline silicon interface of silicon heterojunction solar cells by Raman and FTIR spectroscopy *Adv. Mater.* **35** 2306351
[37] Brodsky M H, Cardona M and Cuomo J J 1977 Infrared and Raman spectra of the silicon-hydrogen bonds in amorphous silicon prepared by glow discharge and sputtering *Phys. Rev. B* **16** 3556–71
[38] Müllerová J, Fischer M, Netrvalová M, Zeman M and Šutta P 2011 Influence of deposition temperature on amorphous structure of PECVD deposited a-Si:H thin films *Cent. Eur. J. Phys.* **9** 1301–8
[39] Mahan A H, Xu Y, Williamson D L, Beyer W, Perkins J D, Vanecek M, Gedvilas L M and Nelson B P 2001 Structural properties of hot wire a-Si:H films deposited at rates in excess of 100 Å/s *J. Appl. Phys.* **90** 5038–47
[40] González N, García T, Morant C and Barrio R 2024 Fine-tuning intrinsic and doped hydrogenated amorphous silicon thin-film anodes deposited by PECVD to enhance capacity and stability in lithium-ion batteries *Nanomaterials* **14** 204
[41] Gritsenko V A, Kruchinin V N, Prosvirin I P, Novikov Y N, Chin A and Volodin V A 2019 Atomic and electronic structures of a-SiNx: H *J. Exp. Theor. Phys.* **129** 924–34

[42] Ingo G M, Zacchetti N, Della Sala D and Coluzza C 1989 x-ray photoelectron spectroscopy investigation on the chemical structure of amorphous silicon nitride (*a* -SiN *x*) *J. Vac. Sci. Technol. A* **7** 3048–55
[43] Ulvestad A, Mæhlen J P and Kirkengen M 2018 Silicon nitride as anode material for Li-ion batteries: understanding the SiNx conversion reaction *J. Power Sources* **399** 414–21
[44] Lovett A J, Füredi M, Bird L, Said S, Frost B, Shearing P R, Guldin S and Miller T S 2025 Structural evolution of silicon nitride anodes during electrochemical lithiation *ACS Electrochem.* **1** 962–73
[45] Ahn D, Kim C, Lee J-G and Park B 2008 The effect of nitrogen on the cycling performance in thin-film Si1−xNx anode *J. Solid State Chem.* **181** 2139–42
[46] Kilian S O and Wiggers H 2021 Gas-phase synthesis of silicon-rich silicon nitride nanoparticles for high performance lithium–ion batteries *Part. Part. Syst. Charact.* **38** 2100007
[47] Ulvestad A, Andersen H F, Mæhlen J P, Prytz Ø and Kirkengen M 2017 Long-term cyclability of substoichiometric silicon nitride thin film anodes for Li-ion batteries *Sci. Rep.* **7** 13315
[48] Ulvestad A, Andersen H F, Jensen I J T, Mongstad T T, Mæhlen J P, Prytz Ø and Kirkengen M 2018 Substoichiometric silicon nitride—an anode material for Li-ion batteries promising high stability and high capacity *Sci. Rep.* **8** 8634
[49] Zhang S 2017 Chemomechanical modeling of lithiation-induced failure in high-volume-change electrode materials for lithium ion batteries *npj Comput. Mater.* **3** 1–11
[50] Beaulieu L Y, Eberman K W, Turner R L, Krause L J and Dahn J R 2001 Colossal reversible volume changes in lithium alloys *Electrochem. Solid-State Lett.* **4** A137
[51] Zhang K, Hüger E, Li Y, Schmidt H and Yang F 2023 Review and stress analysis on the lithiation onset of amorphous silicon films *Batteries* **9** 105
[52] Feyzi E *et al* 2024 A comprehensive review of silicon anodes for high-energy lithium-ion batteries: challenges, latest developments, and perspectives *Energy* **5** 100176